2008

Radio polarimetry studies of magnetic turbulence in supernova remnants

Wendy Jane Stroman
Iowa State University

Radio polarimetry studies of magnetic turbulence in supernova remnants

by

Wendy Jane Stroman

A thesis submitted to the graduate faculty

in partial fulfillment of the requirements for the degree of

MASTER OF SCIENCE

Major: Astrophysics

Program of Study Committee:
Martin Karl Wilhelm Pohl, Major Professor
Lee Anne Willson
E. Walter Anderson
Alex Tuckness

Iowa State University

Ames, Iowa

2008

TABLE OF CONTENTS

LIST OF TABLES

LIST OF FIGURES

Abstract

Polarized radio emission from synchrotron radiation can give us unique information about the structure and amplitude of the magnetic fields in supernova remnants. This has implications for theories of particle acceleration at the forward shock of the SNR, in particular those that involve a strong amplification of the magnetic field through cosmic ray-induced instabilities. This turbulent magnetic field is modeled and I calculate the expected characteristics of polarized synchrotron emission and the effects of Faraday rotation as the radiation propagates through the source. The effects of an underlying homogeneous magnetic field or a compressed shock are also studied. Finally, constraints for realistic parameters describing the magnetic turbulence in the region downstream of the shock are discussed.

CHAPTER 1. INTRODUCTION

1.1 Motivation

The origin of Galactic cosmic rays remains a mystery nearly one hundred years after their discovery. Some theories suggest that strong, turbulent magnetic fields may be required for efficient particle acceleration. Supernova remnants are ideal environments to study these processes as they show evidence of efficient particle acceleration, are expected to contain turbulent magnetic fields directly behind the forward shock, and have known geometries. The goal is to understand the spatial distribution of the turbulence and its effect on the polarization of radio synchrotron emission in the source.

1.1.1 Origin of Galactic Cosmic Rays

The discovery of cosmic rays in 1912 by Victor Hess initiated questions as to their origin and acceleration mechanisms that remain some of the fundamental, unsolved problems in astrophysics today. What is known from various measurements is that our Galaxy contains astrophysical systems capable of accelerating particles to energies far greater than any man-made accelerator.

Cosmic rays are charged particles accelerated to relativistic speeds. Galactic cosmic rays have energies ranging from 10^{10} eV to 10^{15} eV or up to the "knee" of the cosmic-ray spectrum. While cosmic rays consist of both electrons and hadrons, the hadrons account for the majority of the cosmic-ray energy and it is these particles that are the subject of much research. Cosmic rays provide one of only two ways of obtaining matter from outside the heliosphere (the other being interstellar dust), so they are very important to our understanding of the interstellar medium (ISM).

Observations of relativistic, charged particles from the sun interacting with the ISM at the heliosphere show that collisionless shocks are capable of accelerating particles. Indeed, efficient particle acceleration is found to occur in systems with outflow phenomena such as active galactic nuclei (AGN), gamma-ray bursts (GRBs), and supernova remnants (SNRs). Of these, SNRs are the best suited for detailed study because they can be spatially resolved and evolve on convenient timescales, and thus are the focus of this study. Improving our knowledge of the interactions between highly energetic particles and the ISM may help us understand these other systems as well.

1.1.2 Supernova Remnants

The energy density in local cosmic rays, when extrapolated to the whole Galaxy, implies the existence of powerful accelerators in the Galaxy. Supernova remnants appear to be likely candidates to contain such acceleration processes (Ginzburg and Syrovatskii, 1964), but there is no direct evidence that cosmic-ray hadrons are produced in SNRs. The primary argument is that assuming supernova explosions are very efficient at converting their kinetic energy into particles ($\sim 10\% - 20\%$), they are one of only a few types of systems found in our galaxy capable of supplying the necessary energy for cosmic rays (Drury et al., 1989).

Several young shell-type SNRs produce nonthermal X-ray synchrotron emission from accelerated electrons in the 10-100 TeV energy range (Koyama et al., 1995). A few objects have been found to produce GeV-TeV range γ-ray emission (Pohl, 1996; Aharonian et al., 2004). It has been suggested that if SNRs are capable of accelerating electrons to these very high energies, they may be capable of accelerating hadrons as well.

Only in SNRs do we have an opportunity to perform spatially resolved studies in systems with known geometry. Young shell-type supernovae of type Ia are especially suitable for this study because the shock is able to expand isotropically into a near-homogeneous medium. By contrast, core-collapse supernovae (type II and type Ib, Ic) occur only in massive stars whose winds may produce significant inhomogeneity and anisotropy in the environment into which the shock expands.

Observations indicating efficient electron acceleration in SNRs do not, however, imply efficient hadron acceleration. Evidence for this must come directly from signatures of a large flux of high-energy cosmic-ray hadrons in SNRs. This requires a thorough understanding of the observed nonthermal X-ray emission, including the spatial distribution of the magnetic field and both the spatial and energy distributions of high-energy electrons. The scaling of the γ-ray luminosity with that of the synchrotron X-rays depends on the strength and variation of the magnetic field in the source (Pohl, 1996). With this information, the γ-ray emission from accelerated electrons can be modeled to clearly differentiate it from any emission due to accelerated hadrons.

These young shell-type supernovae are expected to contain turbulent magnetic fields associated with the shock. This magnetic field is important in the theory of diffusive shock acceleration, in which particles gain energy by successive crossings of the shock. Kang and Jones (2005) have shown that the process of particle acceleration at supernova shockfronts is intrinsically efficient, which, as discussed above, is necessary for SNRs to account for the observed cosmic-ray energy density.

1.1.3 Magnetic Turbulence

Diffusive shock acceleration is a collisionless process and therefore relies on the interactions between energetic particles and magnetic turbulence. Thus, the study of cosmic-ray acceleration involves the generation, interaction, and damping of magnetic turbulence in a non-equilibrium plasma. The turbulent magnetic field immediately behind the forward shock of SNRs may be much stronger than a typical shock-compressed interstellar magnetic field. The existence of this turbulence remains primarily hypothetical, but it has already been used to model the nonthermal X-ray filaments observed in many SNRs.

High-resolution X-ray observations indicate that a large fraction of the nonthermal X-ray emission from the rims of young SNRs is concentrated in narrow filaments. This is usually interpreted as a large concentration of high-energy electrons at or very near their acceleration site, presumably the forward shock. However, a significant uncertainty in the interpretation

arises from the unknown spatial distribution of the turbulence in the magnetic field.

If hadrons are efficiently accelerated at SNR shock fronts, it is expected that the forward shocks of SNR would be strongly modified with a cosmic-ray induced amplification of the turbulent magnetic field to values much larger than the homogeneous field. To better understand the spatial distribution of the magnetic field, one would look for specific signatures of the magnetic turbulence in the transmission properties of polarized radio synchrotron radiation. Magnetic turbulence can in principle be observed via Faraday rotation and depolarization of these polarized radio waves. Observations of the radio polarization in SNRs do not find evidence for strong Faraday rotation in the source and depolarization by a turbulent magnetic field. Polarization degrees in remnants such as Tycho's are observed to be as high as $20\% - 30\%$ (Dickel et al., 1991).

Detailed simulations show that the acceleration efficacy and the resulting spectra also depend on the orientation angle of the magnetic field and on the amplitude and characteristics of magnetic turbulence near the shock (Giacalone, 2005; Giacalone and Jokipii, 1996). Three-dimensional magnetohydrodynamic (MHD) simulations such as those done by Balsara et al. (2001) do, however, suggest strong depolarization near the forward shocks of SNRs (see figure 1.1).

Clearly the coupled system of magnetic turbulence and energetic particles in a nonequilibrium plasma is an interesting case to study and more detailed analysis is needed. It is hoped that an understanding of particle acceleration in SNRs may solve the question of the origin of Galactic cosmic rays.

1.2 Plan and Goals

The primary goal of this project is to study the spatial distribution of the turbulent magnetic fields in supernova remnants and the effects of this turbulence on the polarization properties of radio synchrotron emission from the source. Current simulations suggest that this region immediately behind the forward shock may be turbulent on size scales smaller than what is resolvable with current telescopes, so I intend to develop a magnetic field that is turbulent on

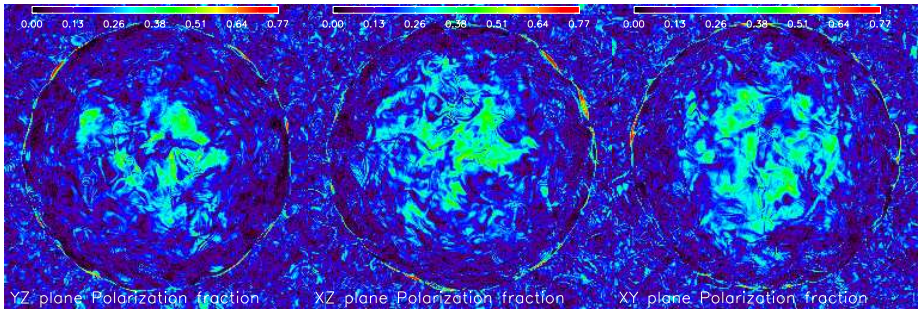

Figure 1.1: 3-D MHD simulations from Balsara et al. (2001) show depolarization near the forward shock for each plane of the simulation.

these small scales in a three-dimensional model.

Since the radiation produced in this region depends on the structure of the magnetic field, I want to calculate the initial polarization properties (degree and direction) at the location it is emitted. It will also be necessary to determine the changes in these quantities due to the turbulent magnetic field causing depolarization and the effects of Faraday rotation as the radiation propagates through the source. The relevant transport equations will be used to trace the polarization of the radiation and the magnetic field through the postshock region. This analysis will provide constraints on what should be observed via the synchrotron radiation if indeed SNRs contain these turbulent magnetic fields.

Additional components that are thought to exist in the downstream regions of SNRs such as an underlying homogeneous field and/or shock compression will be modeled as well. These components may allow the models to more accurately match the observed polarization properties than what is possible with just a simple turbulent field. For clarity, I would note that while the region of interest is behind the forward shock, it is still in front of the contact discontinuity by a fair distance. The results will be compared with current observations of SN 1604 (Kepler's SNR) and SN 1572 (Tycho's SNR) to determine what significance these additional components may have for obtaining realistic parameters for the models.

Providing constraints on the small-scale structure of the post-shock region in SNRs will be useful tools in developing further theories for the origin of Galactic cosmic rays.

CHAPTER 2. BACKGROUND

2.1 Synchrotron Radiation

Relativistic charged particles accelerated by a magnetic field produce synchrotron radiation. Because the particles are moving at relativistic speeds, the emission is strongly beamed in the direction of the instantaneous velocity of the particle, resulting in what is observed as pulses of radiation. The frequency of these pulses are detected as harmonics of the gyration frequency, resulting in a spectrum of radiation. For extremely relativistic particles, the harmonics are so closely spaced that they appear as a continuous power-law spectrum. For more details, see Rybicki and Lightman (1979).

For an ensemble of electrons, the number of electrons per unit volume and per unit solid angle $N(E)$ can be described by the power law: $N(E)dE = KE^{-\delta}dE$. I assume that the electron distribution is homogeneous and isotropic, so rather than using the electron number density, it is more convenient to use the energy distribution of the radiation for which the synchrotron spectral index $n = \frac{1}{2}(\delta - 1)$ is well constrained, and the emissivity $\epsilon \propto \nu^{-n}$.

The emissivity also depends on the perpendicular component of the magnetic field in the emission region:

$$\epsilon(\nu) = a(n) K \frac{\sqrt{3}}{8\pi} \frac{e^3}{mc^2} \left[\frac{3e}{4\pi m^3 c^5}\right]^n (B_\perp)^{n+1} \nu^{-n}, \tag{2.1}$$

where

$$a(n) = 2^{n-1} \frac{n + 5/3}{n+1} \Gamma\left(\frac{3n+1}{6}\right) \Gamma\left(\frac{3n+5}{6}\right) \tag{2.2}$$

(Rohlfs and Wilson, 2004), and K is a constant.

Electrons with energies of ~ 5 GeV produce synchrotron radiation at radio frequencies of a few GHz. Observations of this radio synchrotron emission can be used to probe the structure

of magnetic fields in SNRs. The electric field is predominantly perpendicular to the magnetic-field component in the plane of the sky (Jackson, 1998). An ensemble of electrons produces synchrotron radiation with a degree of linear polarization

$$p = \frac{n+1}{n+5/3} \tag{2.3}$$

which is independent of frequency (Rohlfs and Wilson, 2004; Le Roux, 1961). For typical values of $n = 0.5$ or 0.7 the initial degree of linear polarization is 70% and 72%, respectively. If the magnetic field is turbulent, the polarization direction will vary along the line of sight as well as between neighboring lines of sight. Both of these may cause some depolarization even before Faraday rotation is taken into account.

2.2 Faraday Rotation

A magnetic field applied in the propagation direction of light in an ionized medium will cause the polarization angle to be rotated as in figure 2.1. The motion of free electrons in this medium is a few orders of magnitude greater than that of the ions, so we can neglect the effect of the ions. The light accelerates the thermal electrons and then the Lorentz force acts upon them due to the magnetic field. This causes the electron trajectories to curve, changing the polarization angle of the light. The amount of rotation is proportional to the square of the wavelength, with the proportionality constant usually defined as the Faraday depth of the source. The final polarization angle

$$\chi(\lambda^2) = \psi + \phi\lambda^2, \tag{2.4}$$

where ψ is the initial angle of polarization and ϕ is the Faraday depth defined as (Burn, 1966; Brentjens and de Bruyn, 2005)

$$\phi\left(\mathbf{s}\right) = 0.81 \int_{emitter}^{observer} \left(\frac{n_e}{\mathrm{cm}^{-3}}\right) \left(\frac{\mathbf{B}}{\mu\mathrm{G}}\right) \cdot \left(\frac{d\mathbf{s}}{\mathrm{pc}}\right) \mathrm{rad\,m}^{-2}. \tag{2.5}$$

Note that 1 parsec $\approx 3 \times 10^{18}$ cm. The Faraday depth is positive if the magnetic field is pointing toward the observer and negative if it is pointing away. Figure 2.2 from Brentjens

and de Bruyn (2005) illustrates well how the Faraday depth changes with regard to magnetic field direction and strength and distance along a line of sight.

The synchrotron radiation is emitted within a SNR of finite thickness, so the emission at one location will be rotated by a different degree and in a different direction than the emission from another location. This is likely to result in depolarization of the light. If the magnetic field is turbulent, this will also contribute to the variability of the Faraday depth. Since the amount of rotation would be expected to vary from one line of sight to another, there may be additional depolarization as a result of beam integration.

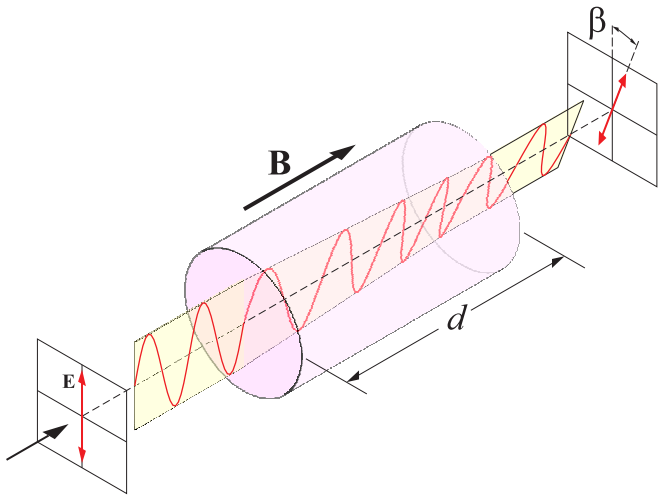

Figure 2.1: As light propagates through an ionized medium a distance d along a magnetic field **B**, the electric field of the radiation **E** is rotated by the angle β, which is defined as $\phi\lambda^2$ in equation 2.4 (Wikipedia, 2008).

2.2.1 Faraday Dispersion Relation

The complex polarized intensity, $P(\lambda^2)$, is defined in Burn (1966) as

$$P(\lambda^2) = \int_{-\infty}^{+\infty} F(\phi) e^{2i\phi\lambda^2} d\phi, \tag{2.6}$$

where $F(\phi)$ is the Faraday dispersion function which describes the emissivity of polarized radiation with respect to Faraday depth. This can be written in terms of the initial degree of

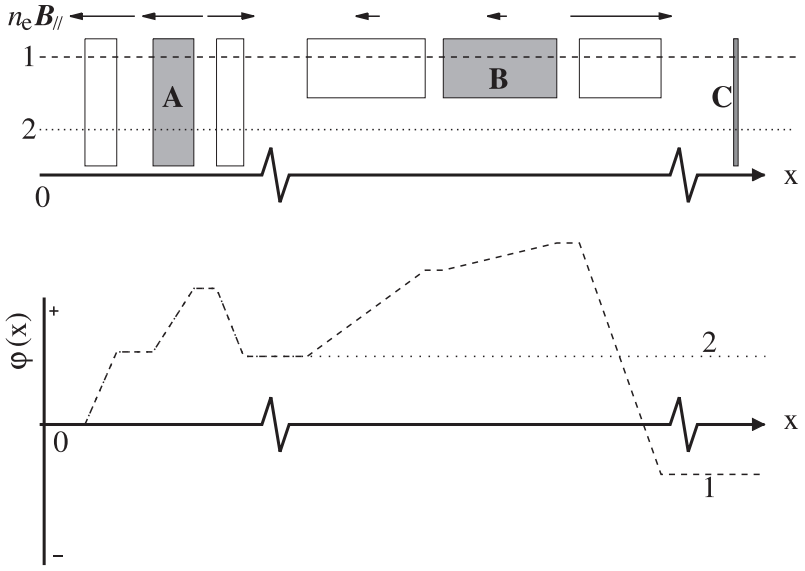

Figure 2.2: Diagram showing the relation between emission regions, $n_e\mathbf{B}_{\|}$, ϕ, line-of-sight position x, and the observed Faraday depth function (Brentjens and de Bruyn, 2005). The observer is at the far left of both plots. The top panel depicts several physical situations. The arrows represent the direction and magnitude of the quantity $n_e\mathbf{B}_{\|}$. White blocks represent areas only containing Faraday rotation. Grey blocks represent areas containing both rotation and emission, except region C which does not have any rotation. There are two lines of sight through these regions, but (2) skips region B. The bottom panel depicts the Faraday depth ϕ as a function of distance for both lines of sight.

polarization (2.3) and the synchrotron emissivity (2.1):

$$F(\phi) = p\frac{dI_\nu}{d\phi}e^{2i\psi} = p\frac{dI_\nu}{ds}\frac{ds}{d\phi}e^{2i\psi} = p\,\epsilon(\nu)\frac{ds}{d\phi}e^{2i\psi}. \tag{2.7}$$

Equation (2.6) can then be written as an integral over ds instead of $d\phi$:

$$P(\lambda^2) = \int_0^\infty p\,\epsilon(\nu, s)e^{2i(\phi(s)\lambda^2+\psi)}ds, \tag{2.8}$$

which allows for the simpler integration of position along the line of sight in the models.

CHAPTER 3. ANALYSIS

3.1 Turbulent Field

A turbulent magnetic field can be constructed via a superposition of many transverse magnetic waves with random orientations. The synchrotron emission is dependent on the structure of this field and is calculated for a range of radio frequencies. Once the model is set up with the spatial distributions of the magnetic field and the synchrotron emissivity, the Faraday depth of the emission can be determined at all points in space. Integrating along the line of sight produces the resulting polarization direction and degree.

3.1.1 Creating a magnetic wave

A single magnetic wave has the form

$$\vec{B} = \vec{B_0} \sin(\vec{k} \cdot \vec{x}) \tag{3.1}$$

and is assumed to fill all space. In order to ensure that $\nabla \cdot \vec{B} = 0$, I employ a method similar to that used in Niemiec and Ostrowski (2006) in which the magnetic field components are chosen to have the form

$$\begin{aligned} B_x &= B_{0,x} \sin(k_y y + k_z z + \sigma_x) \\ B_y &= B_{0,y} \sin(k_x x + k_z z + \sigma_y) \\ B_z &= B_{0,z} \sin(k_x x + k_y y + \sigma_z), \end{aligned} \tag{3.2}$$

where the σ components are randomly generated phase shifts between 0 and 2π.

The projections of the wavevector $\vec{k}$ are:

$$\begin{aligned} k_x &= k \sin\theta \cos\eta \\ k_y &= k \sin\theta \sin\eta \\ k_z &= k \cos\theta \end{aligned} \tag{3.3}$$

such that $k_x^2 + k_y^2 + k_z^2 = k^2$. The random angles θ and η are generated for the projection of $\vec{k}$ in three dimensions such that $-1 \leq \cos\theta \leq 1$ and $0 \leq \eta \leq 2\pi$. The magnitude of $\vec{k}$ is also randomly generated such that $2\pi \times 10^{-3} \leq k \leq 4\pi \times 10^{-1}$. This allows a range of wavelengths between 5 and 1000 cell units, or $20 - 4000$ periods over the line of sight distance.

The magnitude B_0 is defined as

$$B_0 = B_0(k_{min}) \left[\frac{k}{k_{min}}\right]^{\frac{1-q}{2}}, \tag{3.4}$$

where q is the power-law index. For a Kolmogorov spectrum $q = 5/3$ and for a flat spectrum $q = 1$. Both types of models are generated to provide comparisons. I assume that $B_0(k_{min}) = 1\mu$G, a typical value for magnetic fields in the ISM. This is an arbitrary choice and could be adjusted if necessary without consequence to produce a final field with strength similar to that observed in SNRs. The projections are determined in the same way as for $\vec{k}$:

$$\begin{aligned} B_{0,x} &= B_0 \sin\zeta \cos\xi \\ B_{0,y} &= B_0 \sin\zeta \sin\xi \\ B_{0,z} &= B_0 \cos\zeta, \end{aligned} \tag{3.5}$$

except that ζ and ξ are new angles, still randomly generated such that $-1 \leq \cos\zeta \leq 1$ and $0 \leq \xi \leq 2\pi$.

3.1.2 Superposition of waves

It is straightforward to develop a turbulent magnetic field from the superposition of 1000 waves by summing each component as follows

$$B_{x,tot} = \sum_{i=1}^{1000} B_{0x,i} \sin\left(k_{y,i}\, y + k_{z,i}\, z + \sigma_{x,i}\right). \tag{3.6}$$

This results in a magnetic field with turbulence on scales of 5 to 1000 cells, as shown in figure 3.1. For a model wth a Kolmogorov spectrum, the mean magnetic fluctuations $\delta B \approx 10\mu$G while a flat-spectrum model results in $\delta B \approx 20\mu$G. These are of the order of the mean magnetic field strengths observed in young SNRs, so it is not necessary to adjust the initial B_0.

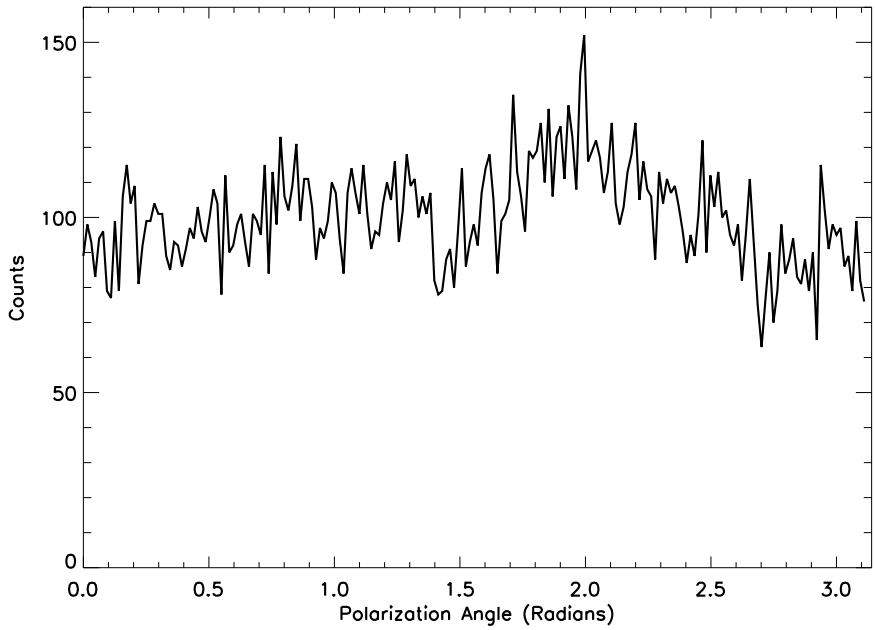

Figure 3.1: Distribution of the initial polarization angles ψ for single line of sight through a turbulent, Kolmogorov magnetic field showing no preferential initial direction.

3.1.3 Coordinate transformations

It is important to make sure that while $\nabla \cdot \vec{B} = 0$ for each wave, the final magnetic field components still fluctuate along all three coordinate axes. To do this, a coordinate transformation is performed three times in order to ensure a random line of sight through the region. This is first done by changing the coordinates (x, y, z) to (x''', y''', z''') via

$$\begin{aligned}
\hat{x}''' &= (\cos\gamma\cos\beta\cos\alpha - \sin\gamma\sin\alpha)\hat{x} + (\cos\gamma\cos\beta\sin\alpha + \sin\gamma\cos\alpha)\hat{y} - (\cos\gamma\sin\beta)\hat{z} \\
\hat{y}''' &= -(\sin\gamma\cos\beta\cos\alpha + \cos\gamma\sin\alpha)\hat{x} - (\sin\gamma\cos\beta\sin\alpha - \cos\gamma\cos\alpha)\hat{y} + (\sin\gamma\sin\beta)\hat{z} \\
\hat{z}''' &= (\sin\beta\cos\alpha)\hat{x} + (\sin\beta\sin\alpha)\hat{y} + (\cos\beta)\hat{z},
\end{aligned} \tag{3.7}$$

where α, β, γ are rotation angles arbitrarily chosen such that no new coordinate axes are parallel to any of the old coordinate axes. Here they are given as $\alpha = \beta = \gamma = \frac{\pi}{4}$. For simplicity, I rename the final coordinates x', y', and z' and give the magnetic field in terms of the new coordinates as

$$\begin{aligned} B_{x'} = B_{0x} \sin(& - k_y(\cos\beta \sin\alpha\, x' - \cos\beta \cos\alpha\, y' + \sin\beta\, z') \\ & + k_z(\sin\beta \sin\alpha\, x' - \sin\beta \cos\alpha\, y' + \cos\beta\, z') \\ & + \sigma_x) \end{aligned} \tag{3.8}$$

and similarly for $B_{y'}$ and $B_{z'}$.

In the new coordinate system, a three-dimensional grid is defined with size 20x20x20000 cells or 50x50x20000 cells. The longest dimension (20000 cells) corresponds to the line of sight, while the other two dimensions are in the plane of the sky.

3.1.4 Synchrotron Emissivity

The synchrotron emissivity in equation 2.1 is calculated directly from the components of the turbulent magnetic field detailed above:

$$\epsilon(\nu) = \left(\sqrt{B_{x'}^2 + B_{y'}^2}\right)^{n+1} \nu^{-n}, \tag{3.9}$$

where all of the constants have been neglected (set equal to 1) because they do not depend on position or frequency. The reasons for this omission will become more clear in the next section.

The range of frequencies measured is 300MHz to 20GHz, although the highest frequencies were dropped from the figures when it was determined that the results did not vary noticeably between 10GHz and 20GHz. There was no significant difference between synchrotron spectral indices of 0.5 and 0.7, so $n = 0.7$ is the index used for the remainder of this analysis.

Depolarization can already be seen from the random polarizations of the emission due to the turbulent magnetic field. The beam-integrated polarization degree is less than 10% even before Faraday rotation is added to the situation. This is the limiting value that the models approach at high frequencies ($\sim$ 10GHz).

3.1.5 Faraday Effects

The Faraday rotation due to the magnetic field is calculated via equation 2.5 for every position in the model. From this, the fraction of polarized intensity of the radiation can be calculated by dividing equation 2.8 by an integral over the total emissivity:

$$P = \left[\frac{\int p\, \epsilon(\nu, s) e^{2i(\phi\lambda^2 + \psi)} ds}{\int \epsilon(\nu, s) ds} \right] \tag{3.10}$$

Since $\epsilon(\nu, s)$ is found in both integrals, it is now clear why the constants from equation 2.1 can be neglected in equation 3.9, as they will cancel each other and only the dependence on s is necessary. The integration of this transport equation proceeds under the constraint that no more than 1° of rotation occurs per step.

This is done by defining the xy-plane of the model as the beam size of 2" (approximately the resolution of the Very Large Array). Then each cell step (ds) in the model corresponds to a physical length of $\sim 5 \times 10^{-4}$ pc. This results in the total line-of-sight distance being $\sim$ 10pc, a reasonable value for most young SNRs in our galaxy. The length of ds determines the maximum wavelength for which the constraint of 1° of rotation holds:

$$\lambda^2 \leq \frac{0.017\,\mathrm{rad}}{0.81\,\mathrm{rad\,m^{-2}}\, B_{z',max}\, n_e\, ds}. \tag{3.11}$$

For the models generated here, $\lambda_{max} = 1$ m or $\nu_{min} = 300$ MHz.

The initial angle of polarization, ψ, is calculated from the components of the magnetic field that are in the plane of the sky:

$$\psi = \arctan\left[\frac{B_{y'}}{B_{x'}}\right]. \tag{3.12}$$

The degree of polarization is given directly by the magnitude of the result in equation 3.10. The final polarization angle is found by calculating $\arctan\left[\Im(P)/\Re(P)\right]$. The results for several models are shown in figures 3.2, 3.3, 3.4, and 3.5.

It is important to remember that the polarization direction calculated is that of the magnetic field as well as the *magnetic component* of the synchrotron radiation, while what is actually observed by a telescope is the electric component of the radiation which is perpendicular to the magnetic component. This will be especially important in sections 3.2.2 and 4.5

where the effects of shock compression are discussed. It is also important to note that the real and imaginary polarization vectors are calculated separately for each line of sight. In order to integrate over an entire beam, the real parts are totaled separately from the imaginary parts before the final degree and angle of polarization is calculated.

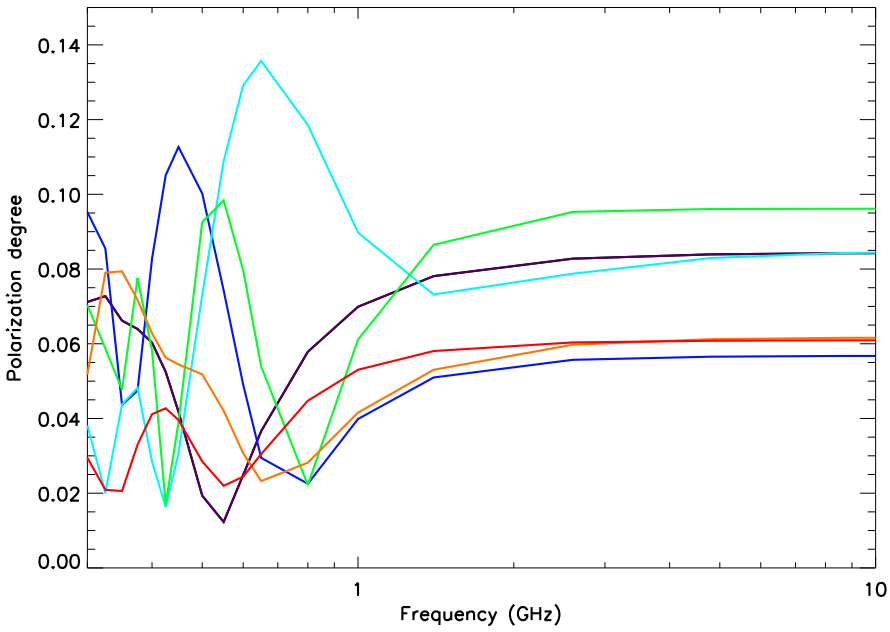

Figure 3.2: Polarization degree as a function of frequency for a selection of six Kolmogorov models.

3.1.6 n_e and δB Variations

It is plausible that the thermal electron density in the region of interest would also have fluctuations. A few tests are performed with electron densities other than 1cm^{-3} to determine whether it is necessary to include a fluctuating density model. These included densities of 10^{-2}cm^{-3}, 10^{-1}cm^{-3}, and 10cm^{-3}. As can be seen in figure 3.6, the result of changing the electron density is to shift this graph to the right or to the left, while the shape of the graph remains the same. Because the Faraday depth depends on the quantity $n_e\, B_{parallel}$, the effect of varying the initial magnetic field strength would be the same as varying the electon density. This confirms that the decision not to explicitly include a fluctuating electron density within

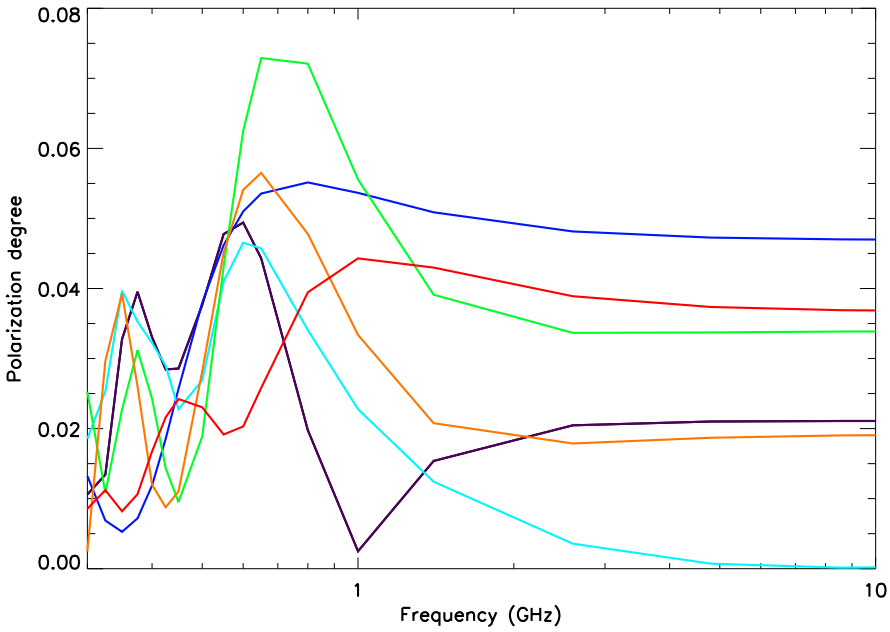

Figure 3.3: Polarization degree as a function of frequency for a selection of six flat models.

the model is acceptable.

3.2 Exploring Additional Parameters

Both theory and observations suggest that a homogeneous field and/or a shock compression may be an important addition to the models. These are addressed below, showing the separate effects of each on the final polarization degree and direction.

3.2.1 Adding a Homogeneous Magnetic Field

A homogeneous magnetic field is added to the turbulent model by increasing the value of one component of the field perpendicular to the line of sight. The x-component was chosen for these cases. The homogeneous field component was added to the turbulent field as 50%, 100%, and 200% of the mean turbulent fluctuations. This was done for both Kolmogorov and flat spectrum models and the results are shown in figures 3.7a and 3.7b.

A homogeneous field with half the strength of the mean turbulent field raises the polariza-

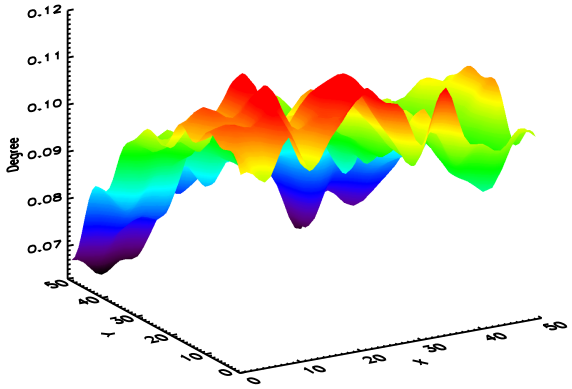

Figure 3.4: Polarization degrees across the beam for a Kolmogorov model at 5GHz.

Model	*Turb. Field*	+50%	+100%	+200%
Flat_01	40.59	8.42	4.21	2.58
Flat_02	0.43	1.92	1.20	0.81
Klm_01	35.59	22.52	5.67	1.85
Klm_02	87.57	12.84	4.13	2.43

Table 3.1: Polarization angles (given in degrees) for models with an additional homogeneous field of different relative amplitude.

tion degree to $12\% - 15\%$ and a field of equal strength to the mean turbulent strength is able to raise the polarization degree to $30\% - 40\%$. The homogeneous field with twice the strength of the turbulent field is rather unrealistic, but included for comparison.

Table 3.1 gives the results for several models with the addition of a homogeneous field of different relative amplitudes. Note that the polarization angles are measured in the counter-clockwise direction with respect to the x-axis. Since the homogeneous field is oriented in the x-direction, the degree to which the total field is aligned parallel to the x-axis is roughly proportional to the strength of the homogeneous field relative to the turbulent field.

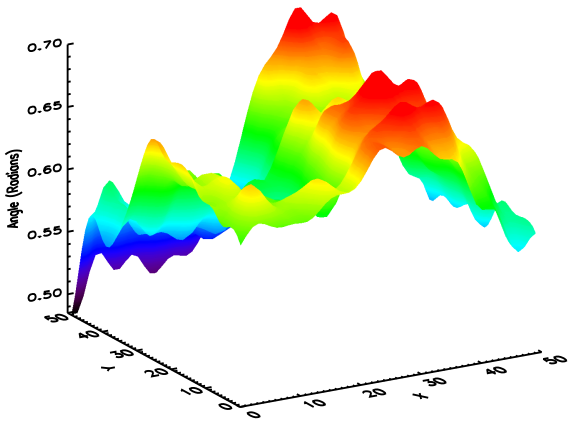

Figure 3.5: Polarization angles across the beam for a Kolmogorov model at 5GHz.

3.2.2 Introducing a Compressed Shock

Another situation to consider is that of a compression in the region of study. Since this region is behind the forward shock, it is likely that the compression ratio would not be as high as at the shock itself ($CR = 4$). More realistic compression ratios for this region are 2-3.

In order to actually simulate a shock compression in the x-direction (the axis perpendicular to the shock front), the number of cells in the x-direction is increased by the compression factor, though the total physical length of that dimension remains fixed. The magnetic field amplitudes in the y- and z-directions are increased by the same factor to produce the physical effect.

The results of this compression are shown in figure 3.8a for the Kolmogorov model and in figure 3.8b for the flat model. The effect of the shock compression on the polarization degree is similar to that of a homogeneous field component, with a ratio of 2 increasing the degree to about 40% and a ratio of 3 increases it to about 55%.

The polarization direction is particularly noteworthy because shock compression is often invoked to explain the radial alignment of the magnetic field observed in many young SNRs. Table 3.2 gives the results for several models with varying compression ratios. Note that the polarization angles are again measured in the counter-clockwise direction with respect to the

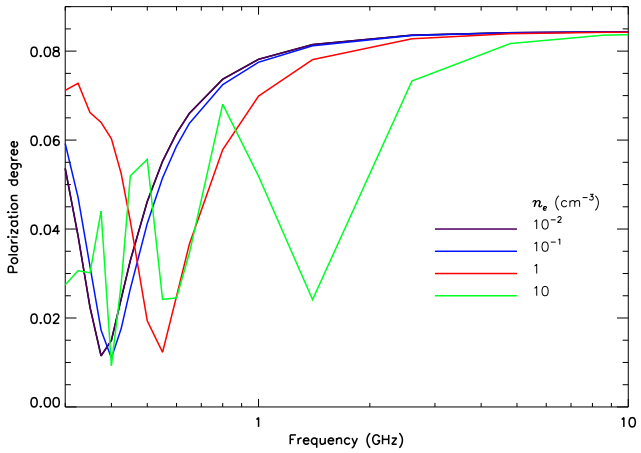

Figure 3.6: Polarization degree as a function of frequency illustrating the effects of changing the thermal electron density by orders of magnitude in a Kolmogorov model. As the electron density is increased, the shape of the plot remains the same but is shifted to the right.

x-axis. As can be seen from this table, the effect of shock compression is to align the field *tangentially*.

Model	$Turb. Field$	$CR = 2$	$CR = 3$
Flat_01	40.59	91.42	93.48
Flat_02	0.43	91.84	92.63
Klm_01	35.59	85.66	89.46
Klm_02	87.57	92.48	93.72

Table 3.2: Polarization angles (given in degrees) for varying compression ratios.

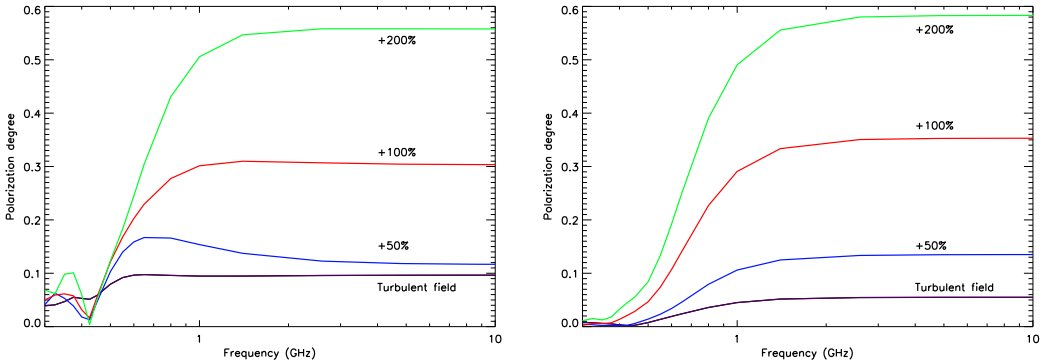

(a) Kolmogorov spectrum (b) Flat spectrum

Figure 3.7: Polarization degree as a function of frequency for models with a homogeneous field component of varying strengths (50%, 100%, and 200% of δB) in the x-direction. A turbulent field without a homogeneous component is included for comparison.

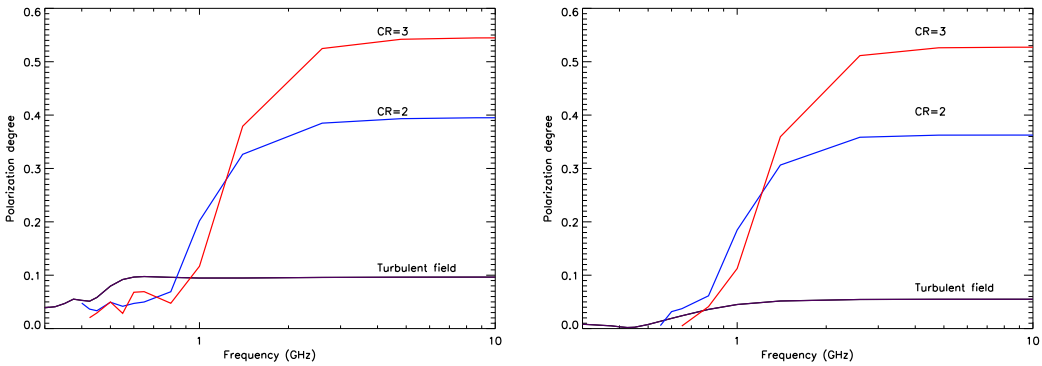

(a) Kolmogorov spectrum (b) Flat spectrum

Figure 3.8: Polarization degrees for models with shock compression ratios CR =2 and 3 and a non-compressed model for comparison.

CHAPTER 4. DISCUSSION

4.1 Comparisons with specific remnants

To determine what constraints are reasonable to expect from these models and in order to analyze the significance of the results, it is important to compare the models with observations of a few shell-type supernova remnants. Two that are well studied are Kepler's SNR (SN 1604) and Tycho's SNR (SN 1572).

Some relevant parameters that have been found for Kepler's SNR are listed in table 4.1. These parameters match well with the parameters chosen in the model. It is also noted here that the models have a smaller beam (2") than was used to observe this remnant. As such, the turbulence in the models are on smaller scales than can be resolved with the current observations.

Figure 4.1 shows a polarization map for Kepler's SNR from DeLaney et al. (2002) indicating that the polarization direction is predominantly radial at the current resolution. As we have seen, this is difficult to reproduce in the models.

Observational parameters for Tycho's SNR are also given, in table 4.2. The polarization and contour map in figure 4.2 (adapted from Dickel et al. (1991)) shows that the shock region (forward shock, contact discontinuity, and reverse shock) is located in the outer $\sim 40\%$ of the remnant's shell. A closer view of the edge of the shock (see figure 4.3 also from Dickel et al. (1991)) shows again that the magnetic field is polarized predominantly in the radial direction. It will be important in future studies to develop explanations for this preferential alignment.

Mean spectral index	-0.71 (6cm - 20cm)
Distance to SNR	4.8 - 6.4kpc
Diameter (distance≈5kpc)	200" or ∼5pc
Beam size	7".2
Compression density ratio	1.8

Table 4.1: Observational properties for Kepler's SNR (DeLaney et al., 2002; Berezhko et al., 2006; Kinugasa and Tsunemi, 2000; Velázquez et al., 2006)

Mean spectral index	-0.8 (6cm - 20cm)
Mean polarization degree in filaments	20%-30%
Distance to SNR	2.5kpc
Diameter	8' or ∼6pc
Beam size	1".5

Table 4.2: Observational properties for Tycho's SNR (Dickel et al., 1991; Wood et al., 1992)

4.2 Flat vs. Kolmogorov Spectrum

The magnetic field spectrum in a supernova remnant is usually assumed to be a Kolmogorov power spectrum, but I have included models with a flat spectrum for comparison. Figure 4.4 shows some examples of the polarization degrees for these models and how they compare to each other.

The overall difference between these two types of models is that flat-spectrum models generally have a lower polarization degree than the Kolmogorov-spectrum models, especially at frequencies above 1GHz. This is primarily due to the fact that the majority of the power in Kolmogorov waves is in the longer wavelengths and thus there is less of the small-scale turbulence which would quickly depolarize the source. However, both of these models produce polarization degrees much less than that observed in remnants such as Kepler's and Tycho's.

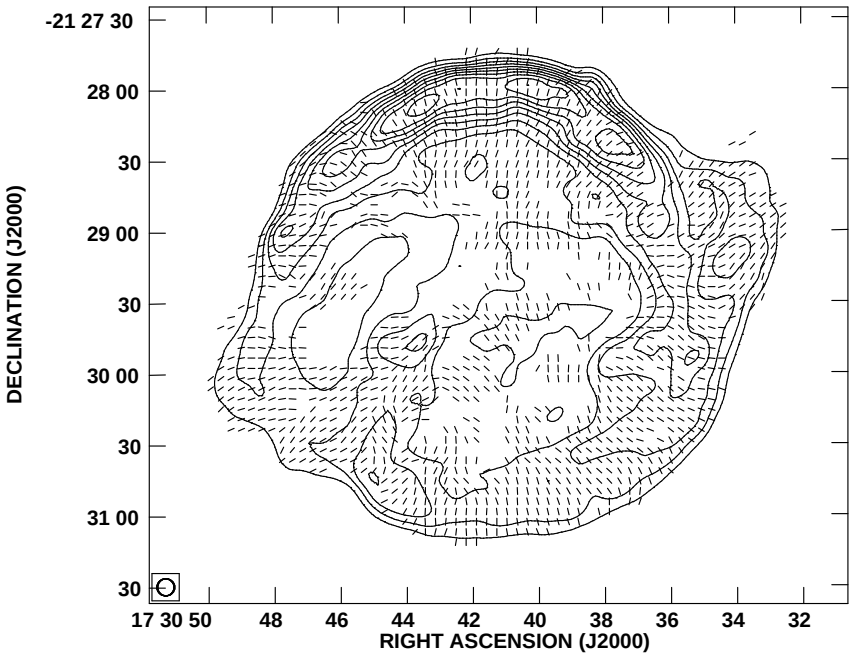

Figure 4.1: Polarization map of Kepler's SNR showing radially-oriented magnetic field near rim of the remnant (DeLaney et al., 2002). The polarization vectors are superimposed on a 6cm total intensity contour map.

4.3 Sources of Depolarization

As was discussed in section 3.1.4, significant depolarization of the synchrotron radiation occurs if a turbulent magnetic field is in the source. This effect is present even in the absence of Faraday rotation and value of the polarization degree is the limiting case as frequency increases to about 10GHz and above.

Integrating over several lines of sight to form a single beam results in an averaging of the lines of sight. As such, it may increase or decrease the polarization fraction when compared with individual lines of sight (see figure 4.5 for an example). This does not appear to greatly affect the mean polarization degree for the model.

The existence of Faraday rotation causes additional depolarization because emission from various distances along the line of sight have varying Faraday depths and are thus rotated by different amounts and in different directions. The effect of rotation is stronger at longer wavelengths. This is also a result of the presence of a turbulent magnetic field within the

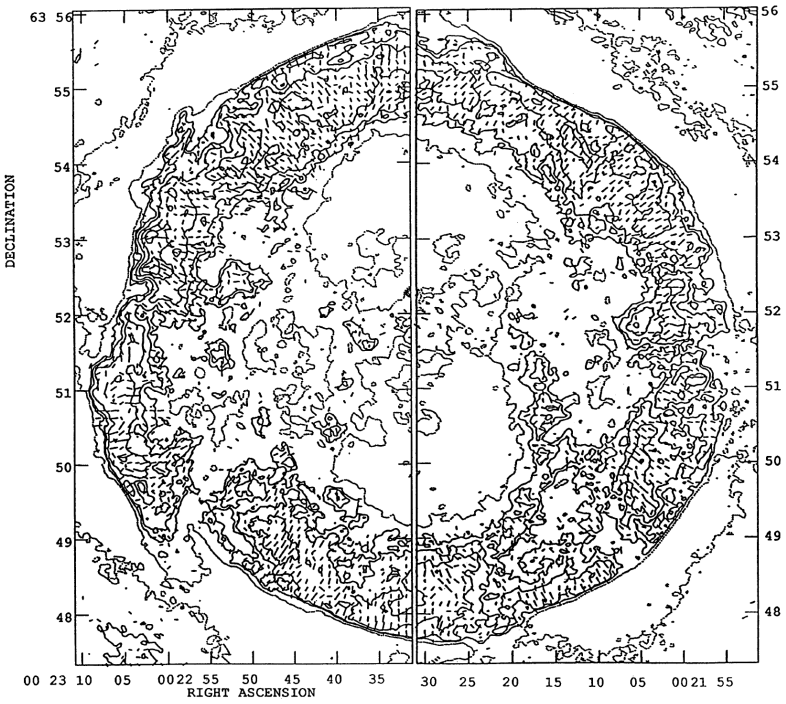

Figure 4.2: Polarization map of Tycho's SNR showing the extent of the shock as the outer 40% of the remnant's radius (Dickel et al., 1991). The polarization vectors are superimposed on a 6cm total intensity contour map.

source.

It is likely a combination of these effects that reduce the polarization degree within the source from the initial $70\% - 72\%$. It appears that they are capable of depolarizing the source by greater amounts than what is observed. Fortunately there are some additional phenomena that are missing from the initial models but have been theorized to be part of the magnetic field structure in the region that may act to increase the polarization degree. These are reviewed in the following sections.

4.4 Homogeneous Magnetic Field

The main effect of adding a homogeneous magnetic field was that it increased the polarization fraction for frequencies above 1GHz. This is shown in figure 3.7. To reproduce the high polarization fractions observed in remnants ($20\% - 30\%$) the necessary amplitude of the

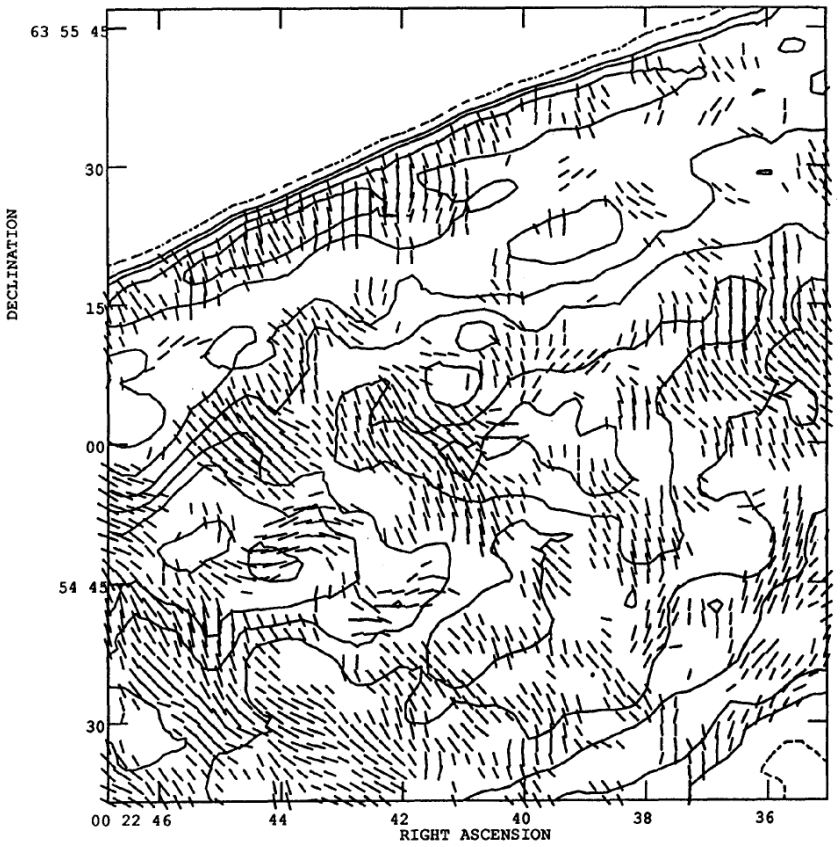

Figure 4.3: Polarization map of close-up section on northeast edge of Tycho's SNR showing radially-oriented magnetic field near rim of the remnant (Dickel et al., 1991).

homogeneous field component would be between 50% and 100% of the mean turbulent field fluctuations.

This is not very realistic, however, since most studies report any underlying homogeneous field as having strength "much less" than the turbulent field component. A homogeneous component of less than $\sim$ 50% is unlikely to add any significant degree of polarization to the source. Thus, the addition of a homogeneous field is not a reasonable explanation of the observed high polarization degrees in SNRs.

Also, the addition of the homogeneous field does not account for the observed radial polarization in the remnants. We would expect the direction of a homogeneous field to be roughly constant over the remnant, since this background field typically varies only on length scales much larger than a single remnant. Therefore, the tendency of the total field to be aligned in

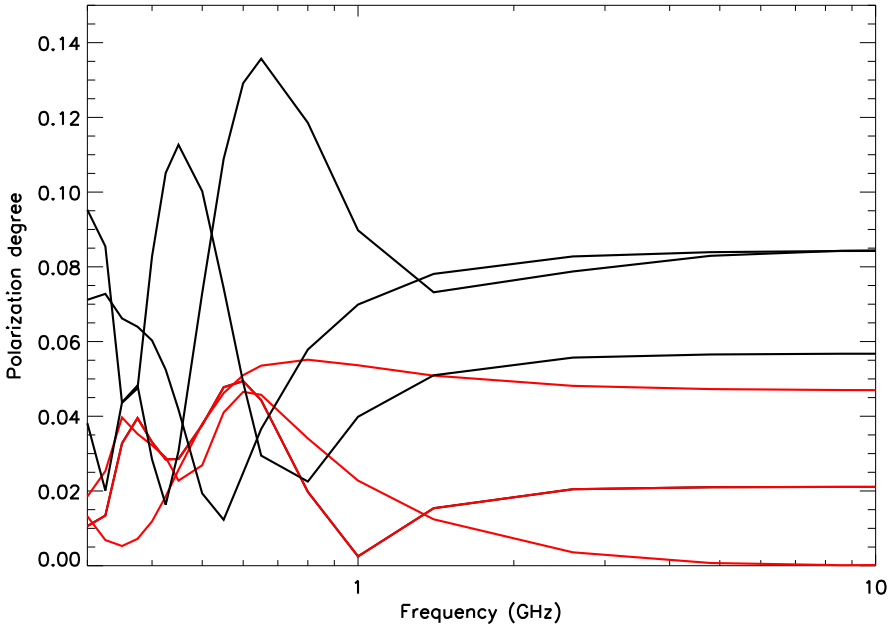

Figure 4.4: Comparison of polarization degrees for flat-spectrum models and Kolmogorov-spectrum models. The black lines correspond to three Kolmogorov models and the red lines correspond to three flat models. In general, the Kolmogorov models have higher degrees of polarization, especially above 1GHz.

the direction of the homogeneous field would cause some areas of the remnant to be radially polarized while others would be tangentially polarized.

4.5 Shock Compression

As discussed in section 3.2.2, the polarization degree for models with a compressed shock (figure 3.8) appear to have similar results as those with the addition of a homogeneous field component. However, unlike the homogeneous field, only a small compression ratio ($CR \leq 2$) is necessary to increase the polarization degree to the levels observed in young SNRs. Because the region is so close behind the forward shock, it is very likely that the compression ratio in this region has a similar value. This is in fact the case for Kepler's SNR as listed in table 4.1. Therefore, a compressed shock may be sufficient to account for the high polarization degrees observed.

The polarization directions in the models, however, do not sufficiently explain the observed

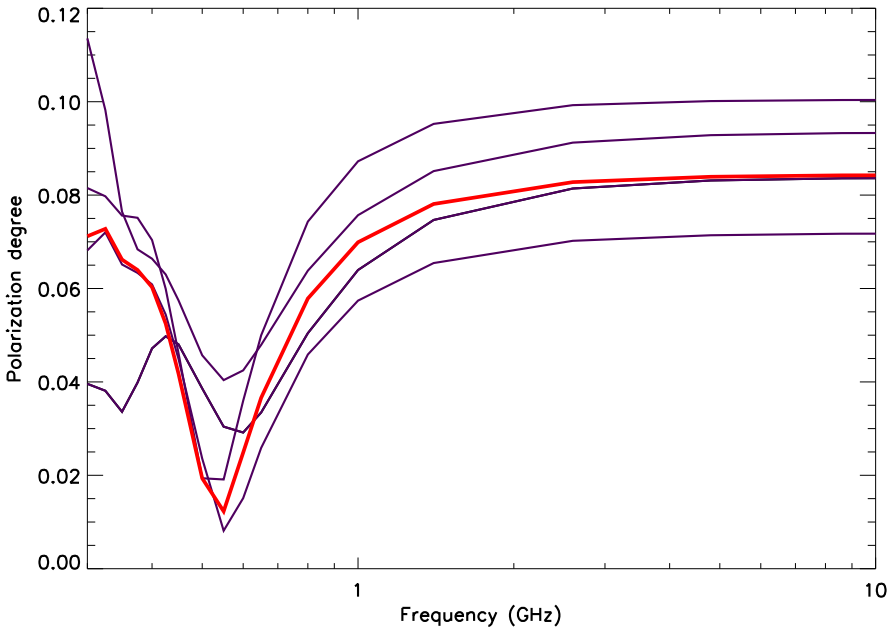

Figure 4.5: A selection of four individual lines of sight and the integrated beam (red line) showing the effect (or rather lack thereof) of beam depolarization for a Kolmogorov model.

radial alignment of the magnetic field in SNRs. As shown in table 3.2, there appears to be a strong correlation between the polarization direction and the compression ratio, but it is perpendicular to the compression direction, rather than parallel. This is expected due to the compression of the tangential component of the magnetic field, but does not allow compression to be a valid explanation for the observed radial alignment.

Bibliography

Aharonian, F. A., Akhperjanian, A. G., Aye, K.-M., Bazer-Bachi, A. R., Beilicke, M., Benbow, W., Berge, D., Berghaus, P., Bernlöhr, K., Bolz, O., Boisson, C., Borgmeier, C., Breitling, F., Brown, A. M., Bussons Gordo, J., Chadwick, P. M., Chitnis, V. R., Chounet, L.-M., Cornils, R., Costamante, L., Degrange, B., Djannati-Ataï, A., Drury, L. O., Ergin, T., Espigat, P., Feinstein, F., Fleury, P., Fontaine, G., Funk, S., Gallant, Y. A., Giebels, B., Gillessen, S., Goret, P., Guy, J., Hadjichristidis, C., Hauser, M., Heinzelmann, G., Henri, G., Hermann, G., Hinton, J. A., Hofmann, W., Holleran, M., Horns, D., de Jager, O. C., Jung, I., Khélifi, B., Komin, N., Konopelko, A., Latham, I. J., Le Gallou, R., Lemoine, M., Lemière, A., Leroy, N., Lohse, T., Marcowith, A., Masterson, C., McComb, T. J. L., de Naurois, M., Nolan, S. J., Noutsos, A., Orford, K. J., Osborne, J. L., Ouchrif, M., Panter, M., Pelletier, G., Pita, S., Pohl, M., Pühlhofer, G., Punch, M., Raubenheimer, B. C., Raue, M., Raux, J., Rayner, S. M., Redondo, I., Reimer, A., Reimer, O., Ripken, J., Rivoal, M., Rob, L., Rolland, L., Rowell, G., Sahakian, V., Saugé, L., Schlenker, S., Schlickeiser, R., Schuster, C., Schwanke, U., Siewert, M., Sol, H., Steenkamp, R., Stegmann, C., Tavernet, J.-P., Théoret, C. G., Tluczykont, M., van der Walt, D. J., Vasileiadis, G., Vincent, P., Visser, B., Völk, H. J., and Wagner, S. J.: 2004, Nature **432**, 75

Balsara, D., Benjamin, R. A., and Cox, D. P.: 2001, ApJ **563**, 800

Berezhko, E. G., Ksenofontov, L. T., and Völk, H. J.: 2006, A&A **452**, 217

Brentjens, M. A. and de Bruyn, A. G.: 2005, A&A **441**, 1217

Burn, B. J.: 1966, MNRAS **133**, 67

DeLaney, T., Koralesky, B., Rudnick, L., and Dickel, J. R.: 2002, ApJ **580**, 914

Dickel, J. R., van Breugel, W. J. M., and Strom, R. G.: 1991, AJ **101**, 2151

Drury, L. O., Markiewicz, W. J., and Voelk, H. J.: 1989, A&A **225**, 179

Giacalone, J.: 2005, ApJ **624**, 765

Giacalone, J. and Jokipii, J. R.: 1994, ApJ **430**, L137

Giacalone, J. and Jokipii, J. R.: 1996, J. Geophys. Res. **101**, 11095

Giacalone, J. and Jokipii, J. R.: 2007, ApJ **663**, L41

Ginzburg, V. L. and Syrovatskii, S. I.: 1964, *The Origin of Cosmic Rays*, The Origin of Cosmic Rays, New York: Macmillan, 1964

Hillas, A. M.: 2005, *Journal of Physics G Nuclear Physics* **31**, 95

Jackson, J. D.: 1998, *Classical Electrodynamics, 3rd Edition*, Classical Electrodynamics, 3rd Edition, by John David Jackson, pp. 832. ISBN 0-471-30932-X. Wiley-VCH , July 1998.

Kang, H. and Jones, T. W.: 2005, ApJ **620**, 44

Kinugasa, K. and Tsunemi, H.: 2000, *Advances in Space Research* **25**, 559

Koyama, K., Petre, R., Gotthelf, E. V., Hwang, U., Matsuura, M., Ozaki, M., and Holt, S. S.: 1995, Nature **378**, 255

Le Roux, E.: 1961, *Annales d'Astrophysique* **24**, 71

Niemiec, J. and Ostrowski, M.: 2006, ApJ **641**, 984

Pohl, M.: 1996, A&A **307**, L57

Rohlfs, K. and Wilson, T. L.: 2004, *Tools of radio astronomy*, Tools of radio astronomy, 4th rev. and enl. ed., by K. Rohlfs and T.L. Wilson. Berlin: Springer, 2004

Rybicki, G. B. and Lightman, A. P.: 1979, *Radiative processes in astrophysics*, New York, Wiley-Interscience, 1979. 393 p.

Velázquez, P. F., Vigh, C. D., Reynoso, E. M., Gómez, D. O., and Schneiter, E. M.: 2006, ApJ **649**, 779

Wikipedia: 2008, *Faraday effect — Wikipedia, The Free Encyclopedia*, [Online; accessed 6-August-2008]

Wood, C. A., Mufson, S. L., and Dickel, J. R.: 1992, AJ **103**, 1338